

Ice front shaping by upward convective current

Ziqi Wang,¹ Linfeng Jiang,¹ Yihong Du,¹ Chao Sun,^{1,2,*} and Enrico Calzavarini^{3,†}

¹*Center for Combustion Energy, Key laboratory for Thermal Science and Power Engineering of Ministry of Education, Department of Energy and Power Engineering, Tsinghua University, Beijing 100084, China*

²*Department of Engineering Mechanics, School of Aerospace Engineering, Tsinghua University, Beijing 100084, China*

³*Univ. Lille, Unité de Mécanique de Lille - J. Boussinesq - UML - ULR 7512, F-59000 Lille, France*

(Dated: January 13, 2023)

The extent and the morphology of ice forming in a differentially heated cavity filled with water is studied by means of experiments and numerical simulations. We show that the main mechanism responsible for the ice shaping is the existence of a cold upward convective current in the system. Such a current is ascribed to the peculiar equation of state of water, i.e., the non-monotonous dependence of density with temperature. The precise form of the ice front depends on several factors, first the temperature difference across the cell which drives the convection, second the wall inclination with respect to the vertical, both of which are here explored. We propose a boundary-layer model and a buoyancy-intensity model which account for the main features of the ice morphology.

Turbulent convective flows along with the ice formation process create intriguing coupling behaviors, which have widespread appearance in nature and strong relevance in industrial applications. In general, the orientation of the temperature gradient and the gravity vector are not parallel. Their angle can play an important role in determining the ice front morphology and the system heat transfer performances, examples are the surfacial icing of lakes and rivers, floating ice bodies (e.g., icebergs), the ice body (e.g., ice shelf) extending outward from the land into waters, and solidification of ice along inclined flow networks in thermal energy storage technology [1–5].

In particular, when the working fluid is freshwater, the coupled physics among the phase change, turbulent convection, as well as the density anomaly (the water density reaches a maximum, ρ_c , at the density peak temperature, T_c ($\sim 4^\circ\text{C}$)) bring more challenges: the gravitational stable and unstable stratification layers coexist, which can strongly influence flow structures.

In recent years, many research efforts have been devoted to furthering the understanding of the dynamical interplay between turbulent convective flows and thermal stratification/phase-transition under different levels of system inclination. Under the scenario of penetrative convection [6], some of these have found that the inclination can induce the breakdown of the fluid stratification which is due to density anomaly of water and there is an optimal tilting angle when the most efficient heat transfer occurs [7–9]. Others have explored the coupling dynamics of phase-change and turbulent convection, they use phase change material (PCM, e.g. Lauric acid) to investigate the heat transfer performance and dynamic thermal behaviors of PCM melting at various system inclination angles [10–12]. However, all these research efforts focused on the system either without phase change or with no density anomaly in consideration. Furthermore, there is still a lack in explorations of the physical mechanisms behind the whole rich ice front morphology. A recent work [4], in a freezing-from-above system, showed that

the density anomaly induced stratification has major effects on the flow structures and the resulting ice front speed and equilibrium state. One may ask the questions: How does the ice front morphology change when the system is tilted? What are the hydrodynamical mechanisms that account for the extent and the complex ice front morphology?

In this work, by combining experiments, numerical simulations, and theoretical modeling, we aim to carry out a systematic exploration of the freshwater solidification, its coupling behavior with the turbulent convective flows, and most importantly, understanding the complex behaviors of the ice front morphology, upon changing the system inclination angle, β . The experiments are conducted in a classical Rayleigh-Bénard (RB) convection system (which is a fluid layer confined between a cold top plate, with temperature, T_t , and a hot bottom plate, with temperature, T_b , and is an ideal system for investigating the rich coupling dynamics mentioned before [14–18]), with a quasi two-dimensional rectangular shape (aspect ratios $L_x/H = 1$ and $L_z/H = 1/4$) (see [Supplementary Information \(SI\) for details](#)). The working fluid is the deionized ultrapure water (Prandtl number, $\text{Pr} \approx 11$). The simulations are performed by means of the CH4-PROJECT code [2], which adopts a Lattice-Boltzmann algorithm for the description of fluid and temperature dynamics, and an enthalpy method for the ice evolution (see [SI for details](#)) [3, 4, 20, 21]. Since the water density inverses at the density peak temperature, T_c ($\approx 4^\circ\text{C}$), here we use the non-monotonous relationship of density with temperature for water near T_c [1], $\rho(T) = \rho_c(1 - \alpha^*|T - T_c|^q)$, with $\rho_c = 999.972 \text{ kg/m}^3$ the maximum density corresponding to $T_c \approx 4^\circ\text{C}$, $\alpha^* = 9.30 \times 10^{-6} (K^{-q})$, and $q = 1.895$. Both in experiments and simulations, the cold plate temperature, T_t , is fixed at -10°C . We first show the comparison of the ice front morphology at the equilibrium state under different heating conditions, T_b , between experiments and simulations, under vertical convection (VC, solidification from left

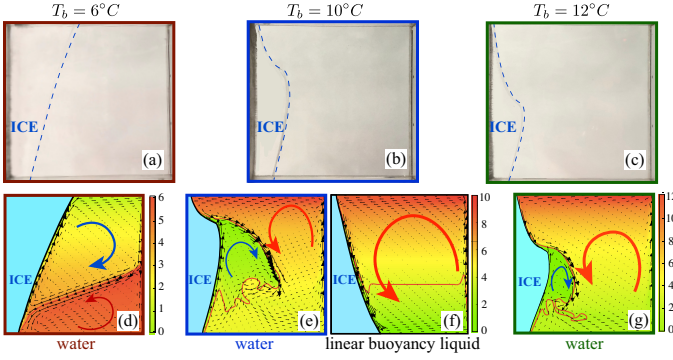


FIG. 1. Comparison of the ice morphology at the equilibrium state under the vertical convection (VC, solidification from left with $\beta = 90^\circ$) in experiments ((a, b, c)), simulations with considering the density anomaly ((d, e, g)), and simulations without considering the density anomaly ((f)). The heating condition is $T_b = 6^\circ\text{C}$ in (a, d); $T_b = 10^\circ\text{C}$ in (b, e, f); $T_b = 12^\circ\text{C}$ in (c, g). (d)-(g) are temperature fields with colors and 0°C (black thick line) and 4°C (red thick line) isotherms, and velocity vectors (black arrows). The red and blue arrows in panels (d)-(g) show the rotating direction of the convective rolls (with stronger convective intensity of thicker arrows).

with $\beta = 90^\circ$). In this study we consider that the equilibrium state is reached when the standard deviation of the spatial-averaged ice thickness time sequence is less than 0.5% with respect to the sequence time-averaged value. Fig. 1(a, b, c) are the experimental results with $T_b = 6^\circ\text{C}$, 10°C and 12°C , respectively (see SI for more experimental results). The corresponding simulation results with properly considering the density anomaly are shown in Fig. 1(d, e, g), which show a good agreement with the experimental results. This indicates that the simulation indeed can capture the correct behavior of the system. For the ice front, counterintuitively, we observe a drastic change of its morphology as T_b increases. This is due to the competition of two convective rolls originating from the density anomaly, i.e., the anticlockwise convective roll (due to the hot plumes detaching from the hot plate, visualized by a red arrow in Fig. 1(d, e, g)) and clockwise convective roll (due to the cold upward convective current along the ice front, visualized by a blue arrow in Fig. 1(d, e, g)). The strength of the rolls can be adjusted by changing T_b . When $T_b = 6^\circ\text{C}$ (Fig. 1(a)), the whole ice is shielded by the upward convective current, and thus the ice front is flat but only tilted. As T_b is increased to 10°C , the ice front becomes highly uneven. The ice is thicker when protected by the upward convective current, thinner at the bottom, and much thinner at the top where the impingement of hot plumes increases the local heat transfer, and consequently, the ice melts more and releases the latent heat to balance the extra coming heat. Further, when T_b is even higher (Fig. 1(c, g)), the anticlockwise roll is much stronger, so it is able to intensively penetrate the clockwise roll and finally af-

fects the ice front morphology, resulting in thinner averaged ice thickness but with a similar shape to the case of $T_b = 10^\circ\text{C}$.

However, the flow structures and ice front profile are highly different when neglecting the density anomaly (i.e., the linear buoyancy liquid with the density as a linear function of the temperature, see Fig. 1(f)): there is only one convective roll, and the ice is flat and tilted which is thinner at the top and thicker at the bottom. There is an extensive bulk region where the temperature is homogeneous and the fluid is quiet. The clear distinction between the simulation with (Fig. 1(e)) and without (Fig. 1(f)) considering the density anomaly indicates that it is crucial to properly consider the real situation of the water. We have observed a similar form of ice front in-

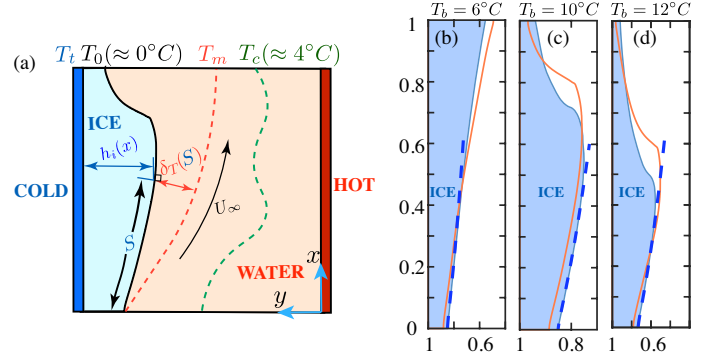


FIG. 2. Boundary layer model to explain the ice front morphology under the VC case. (a) A sketch of the boundary layer model, with black thick line: the ice front (of temperature $T_0 = 0^\circ\text{C}$), red dashed line: the outer boundary of the thermal boundary (of temperature T_m), green dashed line: the T_c isotherm. The flow is of speed U_∞ outside the thermal boundary. (b)-(d) are the comparison of ice front morphology between experiments (blue shaded area), simulations (yellow line) and the model (blue dashed line). The heating condition is (b) $T_b = 6^\circ\text{C}$; (c) $T_b = 10^\circ\text{C}$; (d) $T_b = 12^\circ\text{C}$.

duced by the upward convective current (see Fig. 1(b, c) for experiments as well as (e, g) for simulations). Next, we develop a theoretical model to quantify the trends just described for the freezing front.

We use the concept of thermal boundary layer, which is attached to the ice front, is carved out of the entire flow region, and this is true in that there is always a fluid layer attached to the ice front with the temperature ranging from T_0 to T_c (see the temperature field in Fig. 1(d, e, g)). Fig. 2(a) is a demonstration of the model. The heat is transported in a diffusive way both across the thermal boundary and the ice. When the system reaches an equilibrium state, the heat transferred from the boundary layer into the ice through the ice front balances the heat transferred out of the ice through the cold boundary. Since the ice front (particularly along the initial developing of the thermal boundary layer) is only

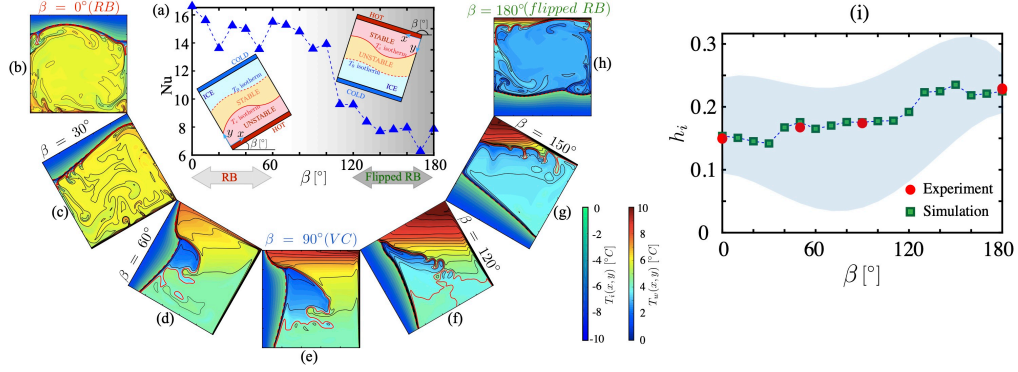


FIG. 3. (a) Nu as a function of β . The error bars are smaller than the symbols. Left (right) inset: the sketch of the arrangement of stably- and unstably-stratified layers of RB (flipped RB) regime with $\beta < 90^\circ$ ($\beta > 90^\circ$). We use the coordinate system attached to the cell. Visualizations of the instantaneous temperature field with colors and isotherms (black thin lines) at the equilibrium state under different β : (b) $\beta = 0^\circ$, (c) $\beta = 30^\circ$, (d) $\beta = 60^\circ$, (e) $\beta = 90^\circ$, (f) $\beta = 120^\circ$, (g) $\beta = 150^\circ$, (h) $\beta = 180^\circ$. The red dashed line and red thick line in panels (b)-(h) are 0°C and 4°C isotherms, respectively. To make the flow structures more visible, two sets of colorbars are used for the temperature field corresponding to the ice region ($T_i(x, y)$) and water region ($T_w(x, y)$). (i) The averaged ice thickness, h_i , as a function of β . Red circles: experiment, green squares: simulation; the blue shaded area shows the spatial variation of the ice thickness. The dashed thin lines connecting the symbols are guide to the eye.

slightly curved, so the thermal boundary layer concept for the flat surface holds in the current situation, and the only modification due to the curvature is geometrical, i.e., δ_T is measured normal to the local ice front surface as a function of the length measured along the ice front, $S(x)$, and $S(x) = \int_0^x \sqrt{1 + \left(\frac{d(h_i(\xi))}{d\xi}\right)^2} d\xi$ (demonstrated in Fig. 2(a)). The energy balance reads,

$$\int_0^{S(x)} k_w \frac{T_m - T_0}{\delta_T(S)} dS = \int_0^x k_i \frac{T_0 - T_t}{h_i(\xi)} d\xi, \quad (1)$$

where k_w and k_i are the thermal conductivity of water and ice, respectively, T_m is the bulk temperature outside the thermal boundary (and $T_m = (T_0 + T_c)/2$), $\delta_T(S(x))$ is the local thermal boundary layer thickness, and $\delta_T(S(x)) = \frac{5.0S(x)}{\sqrt{\text{Re}_x \text{Pr}^{1/3}}}$ [24], with Re_x the external-flow-based Reynolds number, $\text{Re}_x = \frac{U_\infty S(x)}{\nu}$. The velocity scale, U_∞ , is estimated by the free-fall velocity within the fluid between the level of T_0 to that of T_c , and $U_\infty = \sqrt{g[1 - \rho(T_m)/\rho_c]H}$. Since the sidewall is adiabatic, we have $\frac{d(h_i(x))}{dx}|_{x=0} = 0$. To locate the ice front profile, we need an input from the simulation results, i.e., the ice thickness at the starting point of the thermal boundary, h_0 , which is $h_0 = h_0|_{x=0}$. On top of this, the ice morphology can be predicted. Fig.2(b)-(d) show the comparison of ice front morphology among experiments, simulations and model, which shows a good agreement in the region where the upward convective current takes place. Note that the difference at the upper part of the ice front from the simulations and experiments is presumably because the configuration of the convective roll is not exactly the same because of its higher fluctuations which will be discussed below.

Next, we carry out systematical numerical simulations to investigate how β affects the extent and morphology of the ice front, with β from 0° to 180° (here we use the coordinate system attached to the cell). We limit our study to the case of $T_b = 10^\circ$ whose results are easy to extend to other situations.

Firstly, we calculate the heat transfer rate, which when expressed dimensionless is the global Nusselt number, $Nu = (\langle u_y T \rangle - \kappa \partial_y \langle T \rangle) / (\kappa \Delta T / H)$, where $\langle \dots \rangle$ represents an average over time and the whole cell volume, H is the system height. Fig. 3(a) shows the Nu as a function of β . It is noteworthy that there is convection in both $\beta = 0^\circ$ (heating from below) and $\beta = 180^\circ$ (heating from above). Remarkably, when $\beta = 180^\circ$, from the level of T_0 to that of T_c , the fluid is unstably stratified which accounts for creating the convection. We note that the latter feature is specific of water and does not occur in other systems with working fluid that does not possess the density anomaly property, where the density increases with depth.

From Fig. 3(a), it is also observed that the flow changes from highly-turbulent regime with more effective heat transport to weakly-turbulent regime where the heat transfers less efficiently. This is because in RB regime (with small β), the unstably stratified layer is from the level of T_b to T_c (with temperature difference $T_b - T_c \approx 6\text{K}$), while in the flipped RB regime (with large β), the unstably stratified layer is from the level of T_c to T_0 (with temperature difference $T_c - T_0 \approx 4\text{K}$). So on the whole in the flipped RB regime, the thermal driving is weaker.

Fig. 3(b)-(h) show the temperature field with different β from simulations (see SI for more simulation results). The inclination results in different levels of thermal stratification, which induces huge modifications of the ice front morphology. When $\beta = 0^\circ$, there is a stably-

stratified layer (from T_0 to T_c) on top of the unstably-stratified layer (from T_c to T_b). As the cell is tilted with a small β , the convection is strong enough to squeeze the stably-stratified layer to be closely attached to the ice front, so the ice morphology is influenced by the one-roll convective flow (see Fig. 3(b) and (c)). As β increases towards 90° , the inclination of the temperature gradient with respect to the gravity is strong enough to break down the stratification and thus the stably-stratified layer is set into motion in the form of a clockwise convective roll (an upward cold water current) which competes with the initially anticlockwise roll (downward warm water current). The shielding effect is prominent because the ice thickness reaches a local maximum, and the hot plumes impacting on the top part of the ice induces a local minimum of the ice thickness, on top of these two kinds of effects, the ice front presents an inflection point at the transition from the thickest to the thinnest part, which has also been reported in Fig. 1(b) and (c). The flow motion of the original stably-stratified layer intensifies as β increases but still before 90° . After $\beta = 90^\circ$, the stratification configuration flips over. The temperature difference of the unstably-stratified layer is now $(T_c - T_0) \approx 4\text{K}$, which is smaller than that of $\beta < 90^\circ$ (i.e., $(T_b - T_c) \approx 6\text{K}$), so the convective intensity is weaker compared to that before 90° . When $\beta = 180^\circ$, the T_c isotherm is intensively squeezed toward the top hot plate. The unstably stratified layer is directly in contact with the ice front.

To account for the influence of β in a quantitative way, we now calculate the averaged ice thickness, $h_i = \langle h_i(x, y) \rangle_{x,t}$, where $\langle \dots \rangle_{x,t}$ represents an average over time and x-axis direction. Fig. 3(i) reports h_i , as a function of β . There is an increasing trend of h_i as β increases because the heat transfers less efficiently for large β (i.e., flipped RB regime). The results from experiments (red circles) and simulations (green squares) agree well with each other. It is noteworthy that the ice front is highly variable in space as a result of different coupling with the turbulent flow structures. Here, the spatial fluctuations of the ice thickness are represented by the local maximum and minimum of h_i , which is highlighted with the blue shaded area.

Coming back to the cases when β is around 90° , we can observe a peculiar yet robust form of ice front morphology (which can be observed in the range of $\beta = 40 \sim 140^\circ$). In fact, the aforementioned boundary layer model can be extended to the tilted system, by modifying U_∞ , i.e., $U_\infty = \sqrt{(g_x(1 - \rho(T_m)/\rho_c) - g_y\mathcal{H}[\beta - 90^\circ](1 - \rho(T_0)/\rho_c))H}$ where \mathcal{H} is the Heaviside step function. The first term in U_∞ results from the inclination effect, the second part originates from the inherent buoyancy contribution induced by the density difference, and is present only for inclinations larger than 90° . Fig. 4(c)-(m) show the comparison of the ice front morphology between

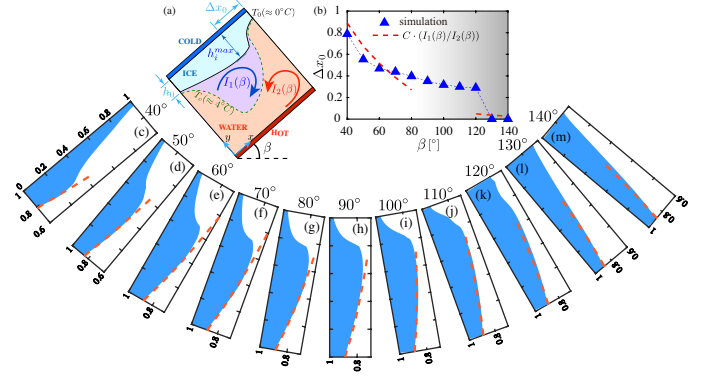


FIG. 4. (a) A sketch of the buoyancy-intensity model to explain the position of the maximum ice thickness. The buoyancy intensity of the clockwise and anticlockwise convective rolls are $I_1(\beta)$ and $I_2(\beta)$, respectively. Δx_0 locates the position of the maximum of the ice thickness. h_0 is the ice thickness at $x = 0$, which is an input parameter of the boundary layer model. h_0 is roughly constant and around the averaged ice thickness, h_i , which is reported in Fig. 3. h_0 as a function of β is reported in SI. (b) Δx_0 as a function of β . (c)-(m) show the comparison of the ice front morphology between the simulation (blue shaded area) and the model (red dashed line) under different β near 90° .

simulations (blue shaded area) and model prediction (red dashed line). It can be observed that the model can capture the behavior of the ice front during the initial development of the thermal boundary. Note that when $\beta < 40^\circ$ and $\beta > 140^\circ$, the boundary layer that is attached to the ice front is disturbed because of the plume impacting under the intensive interaction of the stably- and unstably-stratified layers, so the model cannot be applied. Nevertheless, it is remarkable that the model already performs well in a wide range of β .

Another feature of the ice front is the position, Δx_0 , where the ice thickness reaches the maximum (solid triangles in Fig. 4(b)) and also implies the extent of the hot plume impacting effect. How to understand the trend of Δx_0 ? As has been discussed before, the local maximum of h_i originates from the competition of the buoyancy intensity between two counterrotating rolls. The buoyancy intensity of the cold (clockwise) roll (see the blue arrow in Fig. 4(a)), $I_1(\beta)$, and of the warm (anticlockwise) roll (see the red arrow in Fig. 4(a)), $I_2(\beta)$, can be approximately evaluated with

$$\begin{aligned} I_1(\beta) &= g_x(1 - \frac{\rho(T_m)}{\rho_c}) - g_y\mathcal{H}[\beta - 90^\circ](1 - \frac{\rho(T_0)}{\rho_c}); \\ I_2(\beta) &= g_x(1 - \frac{\rho(T_{m2})}{\rho_c}) + g_y\mathcal{H}[90^\circ - \beta](1 - \frac{\rho(T_b)}{\rho_c}). \end{aligned} \quad (2)$$

where the mean temperature $T_m = (T_0 + T_c)/2$ and $T_{m2} = (T_b + T_c)/2$. Eqn. (2) holds when $\beta \neq 90^\circ$. Plotting the intensity ratio, $C \cdot (I_1(\beta)/I_2(\beta))$, as a function of β , we can obtain an estimation of Δx_0 (red dashed line in Fig. 4(b), and C is a proportionality constant, here $C = 0.076$). This provides further evidence that the

competition of two convective rolls accounts for the form of ice front morphology.

To summarize, we found that the existence of a cold upward convective current, due to the density anomaly of water, accounts for the ice shaping. A boundary-layer model and a buoyancy-intensity model are developed to understand the main features of the ice morphology in a wide range of β . The present exploration offers deeper insight into comprehending the landscape and landforms induced by the coupling behaviors between phase-transition, different levels of thermal stratification in geophysical, meteorological, and ecological systems.

This work was supported by Natural Science Foundation of China under grant nos 11988102, 91852202 and 11861131005.

* chaosun@tsinghua.edu.cn

† enrico.calzavarini@univ-lille.fr

- [1] H. E. Huppert and J. S. Turner, *Nature* **271**, 46 (1978).
- [2] D. Russell-Head, *Annals of glaciology* **1**, 119 (1980).
- [3] E. Rignot, S. Jacobs, J. Mouginot, and B. Scheuchl, *Science* **341**, 266 (2013).
- [4] N. Kousha, M. Hosseini, M. Aligoodarz, R. Pakrouh, and R. Bahrampoury, *Applied Thermal Engineering* **112**, 1497 (2017).
- [5] A. V. Pogorelova, V. L. Zemlyak, and V. M. Kozin, *Journal of Hydrodynamics* (2018).
- [6] G. Veronis, *Astrophys. J.* **137**, 641 (1963).
- [7] H. Inaba and T. Fukuda, *journal of fluid mechanics* **142**, 363 (1984).
- [8] A. Quintino, E. Ricci, S. Grignaffini, and M. Corcione, *International Journal of Thermal Sciences* **116**, 310 (2017).
- [9] A. Quintino, E. Ricci, S. Grignaffini, and M. Corcione, *Heat Transfer Engineering* **39**, 499 (2018).
- [10] B. Kamkari, H. Shokouhmand, and F. Bruno, *International Journal of Heat and Mass Transfer* **72**, 186 (2014).
- [11] B. Kamkari and H. J. Amlashi, *International Communications in Heat and Mass Transfer* **88**, 211 (2017).
- [12] L. Zeng, J. Lu, Y. Li, W. Li, S. Liu, and J. Zhu, *Advances in Mechanical Engineering* **9**, 16878140177220084 (2017).
- [4] Z. Wang, E. Calzavarini, C. Sun, and F. Toschi, *arXiv preprint arXiv:2007.14252* (2020).
- [14] E. D. Siggia, *Annu. Rev. Fluid Mech.* **26**, 137 (1994).
- [15] E. Bodenschatz, W. Pesch, and G. Ahlers, *Ann. Rev. Fluid Mech.* **32**, 709 (2000).
- [16] G. Ahlers, S. Grossmann, and D. Lohse, *Rev. Mod. Phys.* **81**, 503 (2009).
- [17] D. Lohse and K.-Q. Xia, *Annu. Rev. Fluid Mech.* **42**, 335 (2010).
- [18] F. Chillà and J. Schumacher, *Eur. Phys. J. E* **35**, 58 (2012).
- [2] E. Calzavarini, *Software Impacts* **1**, 100002 (2019).
- [20] S. Succi, *The Lattice-Boltzmann equation: for fluid dynamics and beyond* (Oxford university press, 2001).
- [21] C. Huber, A. Parmigiani, B. Chopard, M. Manga, and O. Bachmann, *Int. J. Heat & Fluid Flow* **29**, 1469 (2008).
- [3] B. Rabbanipour Esfahani, S. C. Hirata, S. Berti, and E. Calzavarini, *Phys. Rev. Fluids* **3**, 053501 (2018).
- [1] B. Gebhart and J. C. Mollendorf, *Deep Sea Research Part II Topical Studies in Oceanography* **24**, 831 (1977).
- [24] A. Bejan, *Convection heat transfer* (John Wiley & sons, 2013).

SI: SUPPLEMENTARY INFORMATION

Experiments

The experiments of freshwater solidification in a convective cell with different inclination angles (here we use the coordinate system attached to the cell) are conducted in a classical Rayleigh-Bénard (RB) convection system (see Fig. S1). Fig. S1(a) shows the sketch of the experimental cell. The experimental cell consists of a top cooling plate (with temperature T_t), a heating bottom plate (with temperature T_b), and plexiglas sidewalls with height $H = 240$ mm (length $L_x = 240$ mm and width $L_z = 60$ mm, i.e., aspect ratio $\Gamma = L_x/H = 1.0$). The working fluid, which is confined between the top and bottom plates, is deionized and ultrapure water, and the water density and thermal expansion coefficient around the density peak temperature, $T_c = 4^\circ\text{C}$, are shown in Fig. S1(d) and (e). Before conducting any experiments, water is boiled twice to degas. The temperature of both the top and bottom plates are well controlled at constant temperatures ($T_t < 0^\circ\text{C}$, and $T_b > 0^\circ\text{C}$) by the circulating bath (PolyScience PP15R-40), with the temperature fluctuations less than $\pm 0.2\text{K}$. Silicone O-rings are attached in between the top plate and the sidewall, and also in between the sidewall and the bottom plate, to seal the cell. In order to compensate the volume change during the solidification of freshwater, an expansion vessel is connected to the experimental cell through a rubber tube, which is open to the atmosphere so that the pressure of the experimental cell remains unchanged. Six resistance thermistors (44000 series thermistor element, see the sketch in Fig. S1(c)) are embedded into the top and bottom plates, respectively (see the sketch in Fig. S1(a), the black dots on the top and bottom plates show the placement of the thermistors). There are two steps to avoid the heat exchange between the experimental cell and the surrounding environment, 1) the experimental cell is wrapped in a sandwich structure: insulation foam, aluminum plate (helping to support and acting as the temperature measuring spot of the temperature sensor, PT 100, of the Proportional-Integral-Derivative (PID) system), and insulation foam; 2) a PID (Proportional-Integral-Derivative) controller is used to control the temperature of the surrounding environment outside the experimental cell (see Fig. S1(b)).

During the experiments and numerical simulations, in order to focus on the effect of inclination, we have limited the cold plate to a constant undercooling temperature of $T_t = -10^\circ\text{C}$, which is a typical value in winter. The effects of changing the undercooling temperature, T_t , are qualitatively predictable and are not expected to change the occurrence of different forms of the ice front morphology upon increasing the inclination angle, β , as well as its physical explanation (by the boundary layer theory based model). The only effects that T_t will bring are that, 1) the ice thickness at the equilibrium state of the system is thicker (thinner) with decreasing (increasing) T_t ; 2) the corresponding ice front morphology is similar in the shape compared with that of the current study but will be different in the extension and the local curvature.

We have conducted several typical sets of experiments (we only perform the typical cases of the experiments and did not conduct every experiment corresponding to the simulations because the experiments are time consuming): 1) for investigation of the effects of different heating condition, we have performed $T_b = 6^\circ\text{C}$, 10°C and 12°C , at the system inclination angle of $\beta = 90^\circ$; 2) for the investigation of the influence of the cell inclination, we have done different inclination angles, β , i.e., $\beta = 0^\circ$, 50° , 90° , 180° , at the hot plate temperature $T_b = 10^\circ\text{C}$;

In the experiments, the ice forms on the cold plate and grows in thickness until the system reaches a statistical equilibrium state. The statistical equilibrium state is reached when the standard deviation of the ice thickness time series is less than 0.5%.

Changing the heating condition, T_b can adjust the intensity of the two counterrotating convective rolls. Recall that the water density reaches the maximum, ρ_c , at T_c (which is approximately 4°). Then depending on the value of the hot plate temperature, T_b , the flow configuration can be classified into two regimes:

1) When $4^\circ\text{C} < T_b \leq 8^\circ\text{C}$, the anticlockwise convective roll (with the temperature ranging from T_c to T_b and the corresponding thermal driving $T_b - T_c \leq 4\text{K}$) has weaker intensity than that of the clockwise (with the temperature ranging from T_0 to T_c and the corresponding thermal driving $T_c - T_0 \approx 4\text{K}$). In this regime, the whole ice front is shielded by the colder clockwise roll and is away from the influence of the hot plumes from the hot plate. So the ice front is flat with a tilting angle.

2) When $T_b > 8^\circ\text{C}$, the anticlockwise convective roll (with the temperature ranging from T_c to T_b and the corresponding thermal driving $T_b - T_c > 4\text{K}$) has stronger intensity than that of the clockwise (with the temperature ranging from T_0 to T_c and the corresponding thermal driving $T_c - T_0 \approx 4\text{K}$). So the anticlockwise roll penetrates the clockwise roll and finally affects the ice front morphology, which represents thinner in thickness with higher T_b but similar shape.

With the knowledge of these, we later limited our investigation to the case with $T_b = 10^\circ\text{C}$ and performed more experimental investigation under different inclination angles (see Fig. S2).

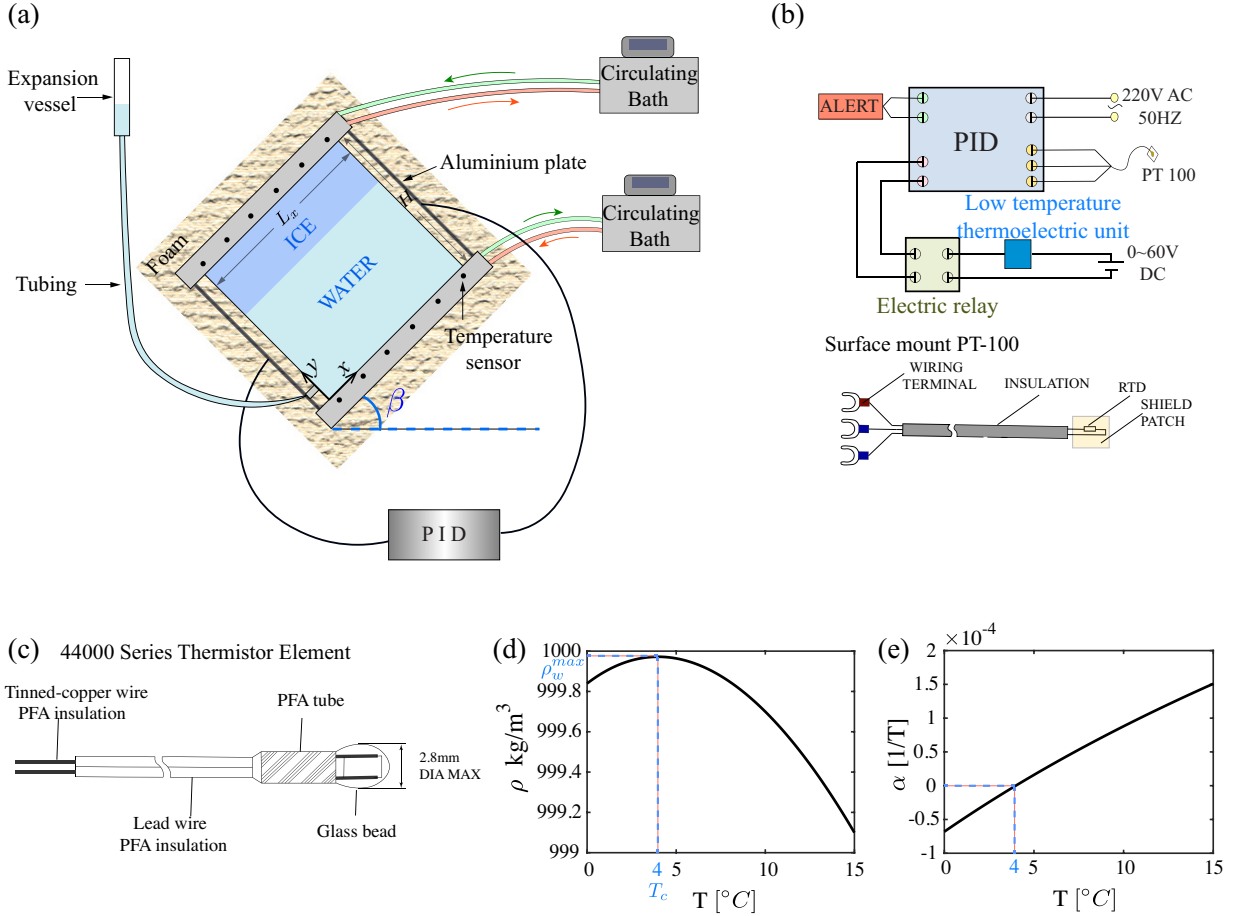


FIG. S1. (a) Sketch of the experimental system for Rayleigh-Bénard convection coupled with solidification of fresh water under different inclination angles. (b) The PID (Proportional-Integral-Derivative) controller and the temperature sensor used in the PID system. (c) The sketch of resistance thermistor, 44000 series thermistor element, which is used to measure the top and bottom plates temperature. (d) The nonmonotonic relationship of the water density with temperature for cold water near T_c from Ref. [1]. (e) the thermal expansion coefficient of water as a function of the temperature.

Fig. S2 reports more experimental results with the parameter $T_b = 10^\circ\text{C}$ and $T_t = -10^\circ\text{C}$, with inclination angle, $\beta = 0^\circ$ (panels (a) and (b)), $\beta = 50^\circ$ (panels (c) and (d)), and $\beta = 180^\circ$ (panels (e) and (f)). Fig. S2(a), (c), and (e) are from experiments, and Fig. S2(b), (d), and (f) are from the corresponding simulations.

From Fig. S3, we can conclude that the results from the experiments and numerical simulations under different inclination angles agree well with each other.

Systematic investigation of various inclination angles

We have conducted a systematical exploration of how β affects the ice morphology, ranging from $\beta = 0^\circ$ to $\beta = 180^\circ$ (here we use the coordinate system attached to the cell). Fig. S3 reports the time sequences of the temperature field under different inclination angles, β with the parameters $T_t = 10^\circ\text{C}$. We focus on the morphology of the ice front at the statistical equilibrium state. In order to speed up the process of reaching an equilibrium state, all the simulations are started with a thin layer of flat ice.

The boundary conditions are no-slip for the velocity, adiabatic at the sidewalls, and constant temperatures at the top and bottom plates. The initial condition is still fluid at linear temperature profile from T_0 to T_b . We assume thermophysical properties to be constant except for the density in the buoyancy term. The real water density property near to the density peak temperature, T_c , is well described with the equation $\rho(T) = \rho_c(1 - \alpha^*|T - T_c|^q)$, with $\rho_c = 999.972 \text{ kg/m}^3$ the maximum density corresponding to $T_c \approx 4^\circ\text{C}$, $\alpha^* = 9.30 \times 10^{-6} (K^{-q})$, and $q = 1.895$. This form of equation gives the maximum density, $\rho_c = 999.972 \text{ kg/m}^3$, at the density peak temperature T_c [1].

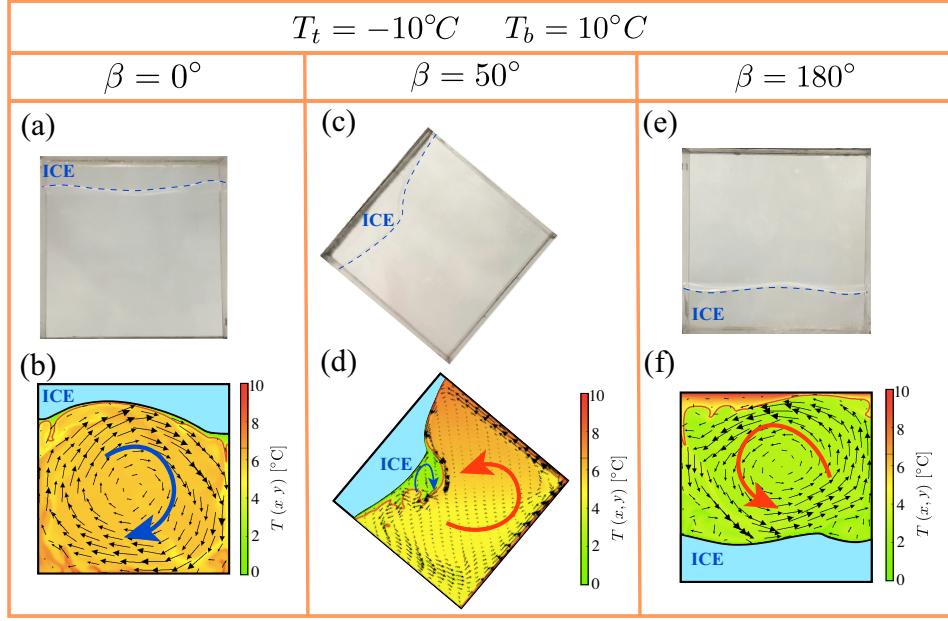


FIG. S2. More results of the experiments ((a), (c), (e)) compared with the simulations (with properly considering the water density anomaly) ((b), (d), (f)). Parameter chosen: (a) and (b): $T_b = 10^\circ\text{C}$ and $\beta = 0^\circ$; (c) and (d): $T_b = 10^\circ\text{C}$ and $\beta = 50^\circ$; (e) and (f): $T_b = 10^\circ\text{C}$ and $\beta = 180^\circ$; The blue dashed line in (a), (c), and (e) shows the ice front position which is guide to the eye. (b), (d), and (f) are the temperature field overlapped with isotherms as well as the velocity vectors. The ice front is represented by the black thick line and the T_c -isotherm is represented by the red thick line. The blue shaded area is the ice layer.

Fig. S3 shows the temperature field (overlapped with isotherms) with varying the system inclination angle, β , from 0° (Rayleigh-Bénard convection with heating from below and freshwater solidification from above) to 180° (flipped Rayleigh-Bénard convection with heating from up and freshwater solidification from below), and here we use the coordinate system attached to the cell. The snapshots at the internal, middle, and outside circles are the temperature field 10min, 2.5hr, and 2.5d (when the system has reached the statistical equilibrium state) after the start of the simulations, respectively. In the RB (small β) and the flipped-RB (large β) regimes, the ice front is heavily affected by the intensive convective flow, and thus the ice front represents complex forms of morphology different from those near the vertical convection cases.

The input parameter of the boundary layer model

It has been mentioned that to locate the ice front profile, we need an input from the simulation results, namely the ice thickness at the starting point of the thermal boundary layer, h_0 , which is calculated by $h_0 = h_0|_{x=0}$. On top of this, the ice morphology can be predicted.

Fig. 4 report the h_0 as a function of the inclination angle, β . It can be observed that h_0 is roughly constant and around the level of the averaged ice thickness h_i , which is shown in Fig. 3 of the main paper..

Introduction to the numerical methods: governing equations and numerical simulations

The simulations are performed by means of the CH4-PROJECT code [2], which adopts a Lattice-Boltzmann algorithm for the description of fluid and temperature dynamics, and an enthalpy method for the ice evolution, which has been intensively validated in [3, 4].

The relevant equations that govern the phase change, the fluid flow, and the heat transfer, as well as the boundary conditions have been discussed in details in our recent work [4]. We focus on the morphology of the ice front at the statistical equilibrium state. In order to speed up the process of reaching an equilibrium state, all the simulations are started with a thin layer of flat ice.

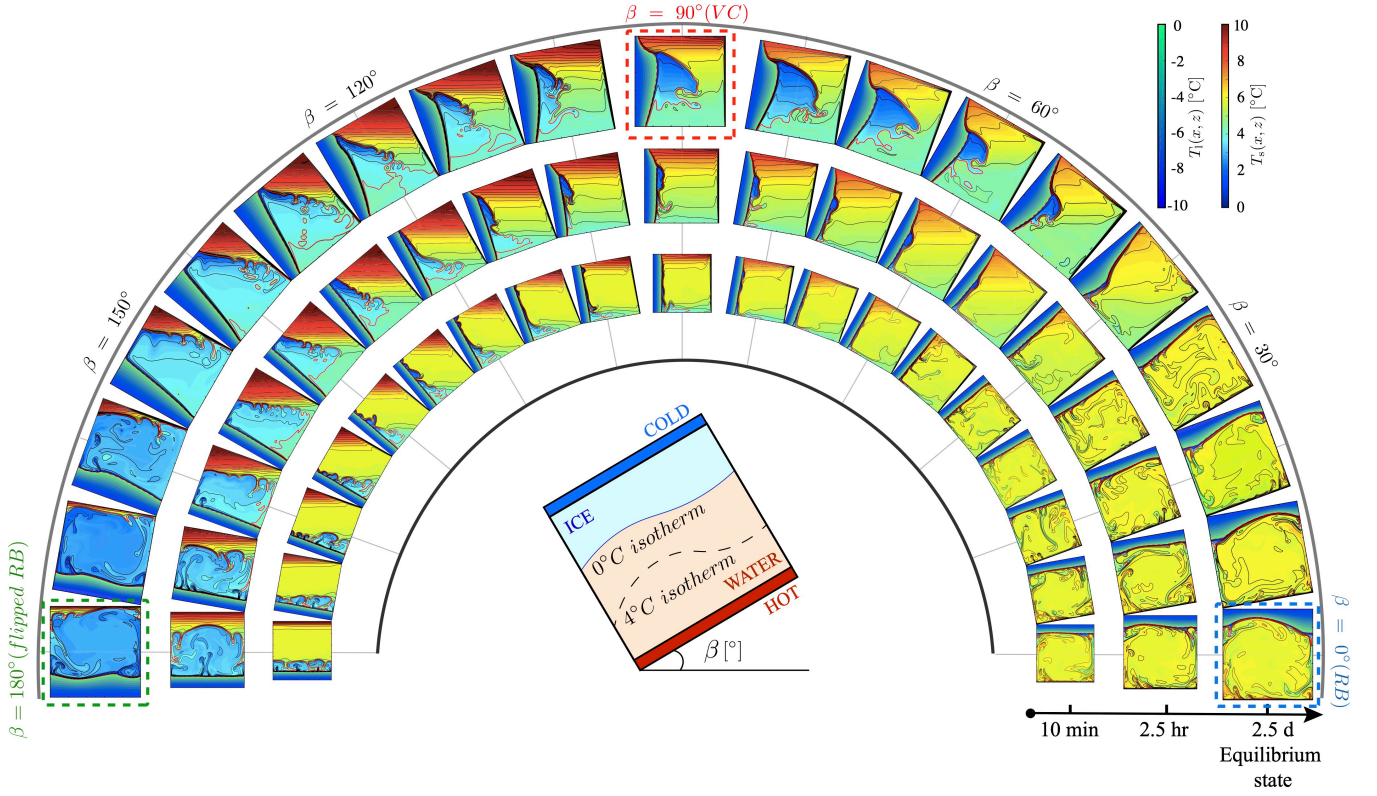


FIG. S3. The systematic investigation of the influence of the inclination angle on the ice front morphology. The snapshots at the internal, middle, and outside circles are the temperature field 10min, 2.5hr, and 2.5d (when the system has reached the statistical equilibrium state) after the start of the simulations, respectively. The black thin lines are the isotherms. The red dashed line shows the ice front, and the red thick line shows the T_c -isotherm. The sketch in the middle shows the coordinate system (attached to the system) and how the inclination angle, β , is defined.

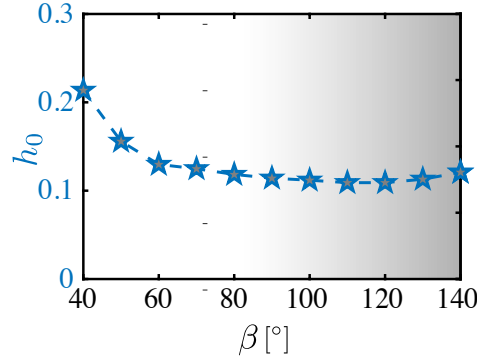


FIG. S4. h_0 as a function of the inclination angle, β . h_0 is the ice thickness at $x = 0$, $h_i|_{x=0}$, which is the input parameter of the boundary layer model.

* chaosun@tsinghua.edu.cn

† enrico.calzavarini@univ-lille.fr

- [1] B. Gebhart and J. C. Mollendorf, Deep Sea Research Part II Topical Studies in Oceanography **24**, 831 (1977).
- [2] E. Calzavarini, Software Impacts **1**, 100002 (2019).
- [3] B. Rabbanipour Esfahani, S. C. Hirata, S. Berti, and E. Calzavarini, Phys. Rev. Fluids **3**, 053501 (2018).
- [4] Z. Wang, E. Calzavarini, C. Sun, and F. Toschi, arXiv preprint arXiv:2007.14252 (2020).